Possible Realization of Optical Quadratic and Dirac Points in Woodpile Photonic Crystals

Hai-Xiao Wang,[1,2,3] Yige Chen,[4] Guang-Yu Guo,[3,5,*] Hae-Young Kee,[4,6,†] and Jian-Hua Jiang[2,‡]

[1] *School of Physical Science and Technology, Guangxi Normal University, Guilin 541004, China*
[2] *School of Physical Science and Technology, & Collaborative Innovation Center of Suzhou Nano Science and Technology, Soochow University, 1 Shizi Street, Suzhou 215006, China*
[3] *Department of Physics and Center for Theoretical Physics, National Taiwan University, Teipei 10617, Taiwan*
[4] *Department of Physics, University of Toronto, Toronto, M5S 1A7, Canada*
[5] *Physics Division, National Center for Theoretical Sciences, Hsinchu 30013, Taiwan*
[6] *Canadian Institute for Advanced Research, Toronto, Ontario, M5G 1Z8, Canada*

The simulation of fermionic relativistic physics, e.g., Dirac and Weyl physics, has led to the discovery of many unprecedented phenomena in photonics, of which the optical-frequency realization is, however, still challenging. Here, surprisingly, we discover that the woodpile photonic crystals commonly used for optical frequency applications host exotic fermion-like relativistic degeneracies: a Dirac nodal line and a fourfold quadratic point, as protected by the nonsymmorphic crystalline symmetry. Deforming the woodpile photonic crystal leads to the emergence of type-II Dirac points from the fourfold quadratic point. Such type-II Dirac points can be detected by its anomalous refraction property which is manifested as a giant birefringence in a slab setup. Our findings provide a promising route towards 3D optical Dirac physics in all-dielectric photonic crystals.

Introduction.— Fermionic relativistic waves described by the Dirac and Weyl equations [1–5] (and beyond [6]) have many nontrivial properties as discovered in condensed materials [7]. Recently, photonic crystals (PCs) became a versatile platform to simulate such relativistic waves [8–23]. Photonic relativistic waves have been harnessed for a number of fundamental phenomena and applications such as *Zitterbewegung* [24], pseudodiffusive transport [25], zero-index metamaterials [26], synthetic magnetic fields for photons [27], and anomalous refraction [17]. In particular, fermion-like relativistic (i.e., even-fold band degeneracy) waves are more appealing than the boson-like (i.e., odd-fold band degeneracy) counterparts, since they are closely related to photonic topological insulators [28–40]. At optical frequencies, the magneto-optical and bianisotropic effects of natural materials, which are often used to create photonic topological insulators, become negligible. One then has to turn to all-dielectric PCs as low-dissipation optical crystalline materials. Recent reports on the experimental observations of photonic Weyl points at the infrared and even optical frequency regimes [18–21] indicate that three-dimensional (3D) dielectric PCs still hold the promise toward Weyl physics. However, realizing 3D optical Dirac points (DPs) as a potential pathway towards optical 3D topological insulators is more challenging, since in PCs the spin degeneracy of photons is broken. Space symmetry must be leveraged to simulate both the fermion-like Kramers degeneracy and the parity inversion [17]. With the limited types of available optical-frequency 3D PCs in the current technology, it is unknown which can lead to 3D photonic DPs.

In this Letter, we illustrate a practical route towards 3D optical DPs: using woodpile-like PCs—a prototype 3D optical-frequency PCs that have been fabricated with high quality [41–46] [Fig. 1(a)]. Surprisingly, we find that the woodpile PCs host two types of exotic band degeneracies in the lowest photonic bands: a Dirac nodal line and a fourfold quadratic point (FQP), as protected by the nonsymmorphic crystalline symmetry. Starting from the motherboard of the woodpile PCs, type-II DPs can be created by deforming the unit-cell geometry. Interestingly, we find that the type-II DPs exhibit anomalous birefringence. Such birefringence is maximized when the incident light excite exactly the type-II DPs. These findings provide a promising path towards optical-frequency Dirac physics and the potential realization of 3D optical topological insulators in all-dielectric PCs that are compatible with optoelectronic integration and nanophotonic applications [44, 47].

Woodpile space symmetry.— Structures of the undeformed and deformed woodpile PCs are illustrated in Figs. 1(a)-(c) together with their unit-cells and lattice vectors. The two corresponding Brillouin zones are illustrated in Fig. 1(d). The deformed woodpile PC has a unit-cell twice as large as the unit-cell of the undeformed woodpile PC. These two PCs can be described in an unified fashion using the unit-cell of the deformed woodpile PC. In this study, we set the lattice constant as $|\vec{b}_1| = |\vec{b}_2| = b_x = 0.8$ μm and $|\vec{b}_3| = b_z = 0.8b_x$. The deformation of the woodpile PC can be feasibly realized by tuning the distances between the dielectric logs, l_x and l_y, or by tuning the width of the logs, w_x and w_y. The undeformed woodpile represents the limit with $w_x = w_y$ and $l_x = l_y = b_x/2$. We consider mostly the woodpile PCs made of TiO_2 which can be directly generalized to other dielectric materials such as silicon and GaAs.

The undeformed woodpile PC is a spiral stacking of

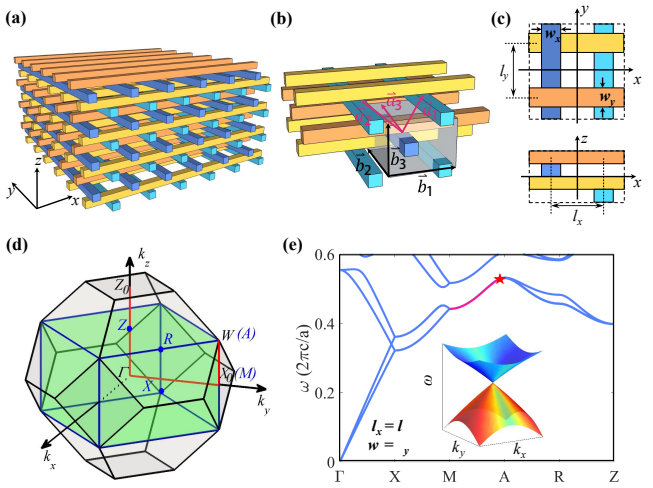

FIG. 1. (Color online) (a) Optical-frequency woodpile PCs: layer-by-layer stacking of dielectric (colored) logs. (b) Lattice vectors of the undeformed woodpile PC, $\vec{a}_j$, are shown together with those of the deformed woodpile PC, $\vec{b}_j$ ($j = 1, 2, 3$). (c) The top-view (upper) and the side-view (lower) of the unit-cell of the deformed (green) woodpile PC. (d) The relationship between the Brillouin zones of the undeformed (gray) and the deformed woodpile PCs. (e) The low-lying photonic bands of the undeformed woodpile PC with $l_x = l_y = b_x/2$, $w_x = w_y = 0.4b_x$, $h = 0.2b_x$, and $\varepsilon = 5.06$ (TiO_2). Inset: the Dirac dispersion at the A point (labeled by the star). The M-A line (red) is a Dirac nodal line on which each point has Dirac-like dispersions.

the dielectric logs, with a four fold screw symmetry $S_{\frac{\pi}{2}} := (x, y, z) \to (y, -x, z + \frac{b_z}{4})$. The space symmetry of the woodpile PCs is elaborated in details in the Supplemental Materials [49]. We list here only the most relevant symmetries: $M_x := (x, y, z) \to (-x - \frac{b_x}{2}, y, z)$ and $M_y := (x, y, z) \to (x, -y - \frac{b_x}{2}, z)$, the glide symmetry $G_z := (x, y, z) \to (x + \frac{b_x}{2}, y, -z - \frac{b_z}{4})$, the fourfold screw symmetries $S_{\frac{\pi}{2}}$, and the point group symmetry $S_4 := (x, y, z) \to (y, -x, -z - \frac{b_z}{2})$. The deformed woodpile PCs may break most of the above symmetries, leaving some of the mirror or glide symmetries unchanged. Note that in this Letter, we use the capital letters for the symmetry operators while the small letters for their eigenvalues.

Symmetry-enriched degeneracy.— Quite different from the simulation of Weyl points, the realization of the synthetic Kramers degeneracy $\mathcal{T}_p^2 = -1$ for photons is crucial for the simulation of the Dirac and quadratic points as well as the Dirac nodal lines. Here, the synthetic Kramers degeneracy is realized via the nonsymmorphic crystalline symmetries. For instance, the double degeneracy on the $k_z = \frac{\pi}{b_z}$ plane [the A-R-Z line in Fig. 1(b)] can be understood by constructing an anti-unitary operator $\Theta_\pi \equiv S_{\frac{\pi}{2}}^2 * \mathcal{T}$ which is invariant at the $k_z = \frac{\pi}{b_z}$ plane and yields $(\Theta_\pi)^2 \Psi_{n,\vec{k}} = e^{ik_z b_z} \Psi_{n,\vec{k}}$ for *all* photonic Bloch states $\Psi_{n,\vec{k}} \equiv (\vec{E}_{n,\vec{k}}, \vec{H}_{n,\vec{k}})^T$ (including both the electric field $\vec{E}$ and the magnetic field $\vec{H}$ for the n-th band with a wavevector $\vec{k}$). Hence, for the $k_z = \pi/b_z$ plane

$$\Theta_\pi^2\big|_{k_z=\frac{\pi}{b_z}} = -1 \tag{1}$$

leads to the synthetic Kramers degeneracy for *all* photonic bands on the $k_z = \frac{\pi}{b_z}$ plane. Similarly, the double degeneracies on the $k_x = \frac{\pi}{b_x}$ [the X-M-A-R line in Fig. 1(b)] and $k_y = \frac{\pi}{b_x}$ planes are induced by the other screw symmetries of the woodpile PCs (see Supplemental Materials [49] for details).

Photonic Dirac nodal line.— The M-A line is a nodal line composed of an "infinite" number of two-dimensional (2D) DPs [see Fig. 1(e) and Fig. 2]. The two fundamental elements in the Dirac equation, the spin and orbital degrees-of-freedom, are associated with the four degenerate states on the line. The field profiles of these four modes [Fig. 2(a)] indicate that they are the electric and magnetic dipole modes which can be denoted by the mirror quantum number as $|m_x, m_y\rangle$ ($m_x, m_y = \pm 1$). The fourfold degeneracy is dictated by $\Theta_z \equiv G_z * \mathcal{T}$ and $S_\pi \equiv S_{\frac{\pi}{2}}^2$ which are invariant operators on the M-A line, as manifested by the following symmetric transformations (see Supplemental Materials for more details [49]),

$$\Theta_z|m_x, m_y\rangle = |-m_x, m_y\rangle, \tag{2a}$$
$$S_\pi|m_x, m_y\rangle = |-m_x, -m_y\rangle, \tag{2b}$$
$$\Theta_z S_\pi|m_x, m_y\rangle = |m_x, -m_y\rangle. \tag{2c}$$

Here, the "orbital" degree-of-freedom are associated with the *parity*, $\mathcal{P} = m_x m_y$. For example, the two electric dipole modes $|m_x = -1, m_y = 1\rangle$ and $|m_x = 1, m_y = -1\rangle$ constitute the odd-parity "antiparticle" sector of the Dirac equation, whereas the magnetic dipole modes $|1, 1\rangle$ and $|-1, -1\rangle$ comprise the even-parity "particle" sector. The "spin" states for the particle sectors ('p') and antiparticle ('a') are constructed, respectively, as

$$\begin{aligned}
|p, \uparrow\rangle &= \frac{1}{\sqrt{2}}(|1, 1\rangle + i|-1, -1\rangle) \equiv \frac{|x^2 - y^2\rangle + i|2xy\rangle}{\sqrt{2}}, \\
|p, \downarrow\rangle &= \frac{1}{\sqrt{2}}(|1, 1\rangle - i|-1, -1\rangle) \equiv \frac{|x^2 - y^2\rangle - i|2xy\rangle}{\sqrt{2}}, \\
|a, \uparrow\rangle &= \frac{1}{\sqrt{2}}(|-1, 1\rangle + i|1, -1\rangle) \equiv \frac{|x\rangle + i|y\rangle}{\sqrt{2}}, \\
|a, \downarrow\rangle &= \frac{1}{\sqrt{2}}(|-1, 1\rangle - i|1, -1\rangle) \equiv \frac{|x\rangle - i|y\rangle}{\sqrt{2}}.
\end{aligned} \tag{3}$$

In the above equations, we have denoted the mirror eigenstates as $|-1, 1\rangle \equiv |x\rangle$, $|1, -1\rangle \equiv |y\rangle$, $|1, 1\rangle \equiv |x^2 - y^2\rangle$ and $|-1, -1\rangle \equiv |2xy\rangle$ to elucidate the spatial symmetry of the eigenstates. We find that the two spin states carry finite and opposite *total angular momenta* (including both spin and orbital angular momentum) of photon (see Supplemental Materials [49]), which is a natural generalization

of the concept of emulating fermion-like spin with photonic spin [33] or orbital angular momentum [36, 38] in previous studies.

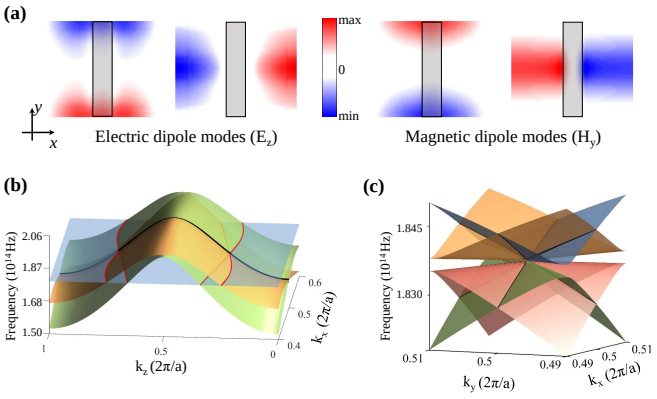

FIG. 2. (Color online) (a) Field profiles of the four degenerate modes on the M-A line. (b) and (c): Dispersion of the Dirac nodal line in the (b) k_x-k_z and (c) k_x-k_y planes. In (b) an isofrequency plane (the blue-gray sheet) is plotted in order to show the isofrequency contours (the red curves). The Dirac nodal line is labeled by the black curve. Parameters are the same as in Fig. 1.

Photonic simulation of a fermionic Hamiltonian $\hat{\mathcal{H}}_F$ is the following mapping from the photonic Hamiltonian $\hat{\mathcal{H}}_{EM}$ to the fermionic one (resembling the mapping between the Dirac equation and the Klein-Gordon equation [48]),

$$\hat{\mathcal{H}}_{EM} := (\hat{\mathcal{H}}_F)^2. \tag{4}$$

From the Maxwell equation, $c^2\boldsymbol{\nabla}\times\frac{1}{\varepsilon}\boldsymbol{\nabla}\times\vec{H}=\omega^2\vec{H}$ (c is the speed of light in vacuum, ε the relative permittivity, and $\vec{H}$ is the magnetic field), the photonic Hamiltonian can be defined as the Hermitian operator $\hat{\mathcal{H}}_{EM} := c^2\boldsymbol{\nabla}\times\frac{1}{\varepsilon}\boldsymbol{\nabla}\times$ [45].

In the basis of the four states, $|\rho,\uparrow\rangle$, $|\rho,\downarrow\rangle$ ($\rho=a,p$), the above mapping (together with the $\vec{k}\cdot\vec{P}$ theory) yields the following fermion-like Hamiltonian,

$$\hat{\mathcal{H}}_F^{DL} = \omega_0 + v\begin{pmatrix} 0 & \hat{\mathcal{A}} \\ \hat{\mathcal{A}}^\dagger & 0 \end{pmatrix}, \tag{5}$$

Here $\hat{\mathcal{A}}\equiv\gamma_x q_x\sigma_x+\gamma_y q_y\sigma_y$, and $q_j=k_j-\pi/b_x$ ($j=x,y$). The coefficients ω_0, v, γ_x and γ_y are k_z-dependent, making the Dirac nodal line. At the M and A points, the S_4 symmetry imposes additional constraints, $\gamma_x=\gamma_y$, leading to an isotropic 2D DP as shown in Fig. 1(e). Away from these two points, the S_4 symmetry is ineffective, yielding unconventional 2D DPs as shown in Fig. 2(c).

Since the particle and antiparticle sectors correspond to the magnetic and electric dipole modes, respectively, the magneto-electric coupling in the Maxwell equations naturally guarantee the linear in $\vec{q}$ "spin-orbit couplings". The coupling coefficients can be written as (Here, $j=x,y$, and UC stands for the unit cell)

$$v\tilde{\gamma}_j = \frac{c}{\sqrt{N_E N_H}}\int_{UC} d\vec{r}\,(\vec{E}^*_{\uparrow,p}\times\vec{H}_{\downarrow,a}+\vec{E}_{\downarrow,a}\times\vec{H}^*_{\uparrow,p})\cdot\vec{n}_j,$$

where $\tilde{\gamma}_x=\gamma_x$ and $\tilde{\gamma}_y=-i\gamma_y$; $N_E\equiv\int_{UC}d\vec{r}\varepsilon(\vec{r})|\vec{E}|^2$,$N_H\equiv\int_{UC}d\vec{r}|\vec{H}|^2$; $\vec{n}_j$ is the unit vector along the $j=x,y$ direction; the integration is within a unit-cell. Interestingly, the above expression is similar to the Poynting vector between the particle and antiparticle sectors. A general form of the Dirac velocity tensor is presented in Supplemental Materials [49] where the "selection rules" due to the mirror and glide symmetries are discussed.

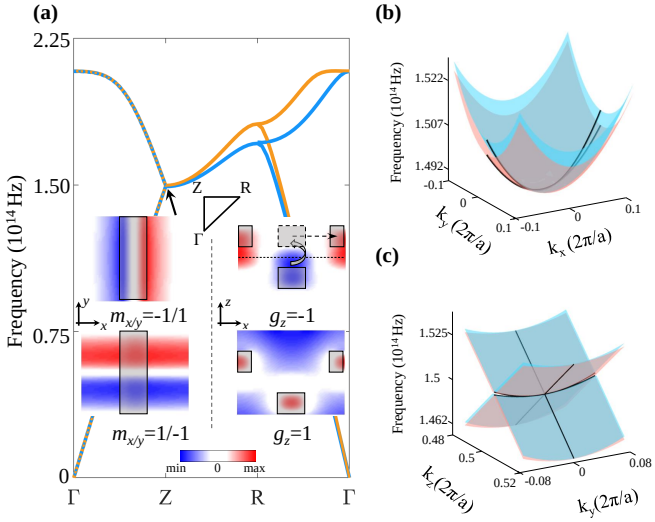

FIG. 3. (Color online) Quadratic degeneracy points: (a) Photonic bands in the $k_y=0$ plane for the same parameters as in Fig. 1. The orange (blue) band has $m_y=+1$ (-1). The Z point (indicated by the arrow) is a FQP with four eigenstates of different mirror ($m_{x/y}$) and glide (g_z) symmetries (illustrated in the inset). (b) and (c): Dispersion of the FQP in the (b) k_x-k_y and (c) k_y-k_z planes.

Photonic fourfold quadratic point.— The Z point is a photonic FQP which is induced by the fourfold screw symmetry $S_{\frac{\pi}{2}}$ as

$$(\Theta_{\frac{\pi}{2}})^4 = e^{ik_z b_z}\big|_{k_z=\frac{\pi}{b_z}} = -1, \tag{6}$$

where $\Theta_{\frac{\pi}{2}}\equiv S_{\frac{\pi}{2}}*\mathcal{T}$ transforms (k_x,k_y,k_z) to $(-k_y,k_x,-k_z)$ and is an invariant operator at the Z point. The above indicates that the quadruplet consist of $|\Psi\rangle$, $\Theta_{\frac{\pi}{2}}|\Psi\rangle$, $(\Theta_{\frac{\pi}{2}})^2|\Psi\rangle$, and $(\Theta_{\frac{\pi}{2}})^3|\Psi\rangle$. If $|\Psi\rangle$ is labeled as $|m_x,m_y,g_z\rangle$ ($g_z=\pm1$ is the eigenvalue of G_z), then

$$\Theta_{\frac{\pi}{2}}|\Psi\rangle=|m_y,m_x,g_z\rangle,\quad (\Theta_{\frac{\pi}{2}})^2|\Psi\rangle=|m_x,m_y,-g_z\rangle,$$
$$(\Theta_{\frac{\pi}{2}})^3|\Psi\rangle=|m_y,m_x,-g_z\rangle. \tag{7}$$

The field patterns of the eigenstates are shown in Fig. 3(a), indicating $m_x = -m_y$. The fourfold degeneracy at the Z point is protected by the screw symmetry $S_{\frac{\pi}{2}}$ and hence independent of the specific parameters of the woodpile PC (see Supplemental Materials [49]).

The photonic system simulates the following fermion-like Hamiltonian of a 3D FQP,

$$\hat{\mathcal{H}}_F^Z = \omega_Z + v_z q_z \hat{\tau}_y + f_0[(q_x^2 - q_y^2)\hat{\sigma}_z + 2f_1 q_x q_y \hat{\sigma}_x + f_2 q_\parallel^2], \quad (8)$$

where ω_Z is the frequency at the Z point, v_z is the group velocity along the z direction, and $q_z = k_z - \frac{\pi}{b_z}$. $\tau_z = \pm 1$ labels the $g_z = \pm 1$ states, while $\sigma_z = \pm 1$ labels the $m_y = \pm 1$ states. The coefficients f_i $(i = 0, 1, 2)$ depend on the geometry and materials of the PC (see Supplemental Materials [49] for details).

Photonic Dirac points.— There are two means to split the FQP to yield a pair of DPs: either tuning w_y/w_x or l_y/l_x away from unity. For these tuning, $S_{\frac{\pi}{2}}$ is broken while $(\Theta_{\frac{\pi}{2}})^2 = S_\pi$ is preserved. From Eq. (7), the degeneracy between states of different $m_{x/y}$ is then lifted. This can be described by a constant perturbation $\Delta_z f_0 \sigma_z$ that splits the FQP to a pair of DPs emerging at two wavevectors $\vec{K}_\pm = (0, K_y^\pm, \frac{\pi}{b_z})$ with $K_y^\pm = \pm\sqrt{|\Delta_z|}$. The DPs are described by the following Hamiltonian,

$$\hat{\mathcal{H}}_F^{DP\pm} = \omega_D \pm v_0 \delta k_y + v_z \delta k_z \hat{\tau}_y \pm v_x \delta k_x \hat{\sigma}_x \pm v_y \delta k_y \sigma_z, \quad (9)$$

where $\vec{\delta k} = \vec{k} - \vec{K}_\pm$. Here, the coefficients are given by $\omega_D = \omega_Z + f_2 f_0 |\Delta_z|$, $v_0 = 2f_2 f_0 K_y^+$, $v_x = 2f_1 f_0 K_y^+$, and $v_y = -2f_0 K_y^+$. With the parameters adopted, we find that $|v_0| > |v_y|$, thus the Dirac cones are of the type-II nature [see Fig. 4(a)] (see Supplemental Materials [49]).

Anomalous refraction.— The band degeneracies have been detected via transmission measurements [9, 11, 18–21]. Here, we show that they can also be detected via unconventional refraction, specifically, the birefringence. Birefringence emerges here because the type-II DPs support two branches of propagating refraction beams with different group velocities. The setup for measuring the birefringence is illustrated in Fig. 4b. A Gaussian beam is shed on the PC slab and is detected at the bottom of the slab. The drifted beam centers at the detection plane, $\vec{r}_o = r_o(\cos\phi_o, \sin\phi_o)$, gives the azimuth refraction angle ϕ_o. In the theory of refraction, the wavevector in the PC is determined by frequency and parallel wavevector matching. We find that the refraction angle is determined by the group velocities as $\phi_o = \arctan(v_{g,y}/v_{g,x})$ and $\theta_o = \arctan(\sqrt{v_{g,x}^2 + v_{g,y}^2}/v_{g,z})$.

Considering refraction on the (001) surface, type-II dispersion yields birefringence with two refraction beams [17], characterized by two displacement vectors $\vec{r}_{o,\pm}$. We show that the DPs can be detected by studying the difference in the azimuth refraction angle $\delta\phi_o \equiv |\phi_{o,+} - \phi_{o,-}|$. Fig. 4(c) shows that the DP at $\vec{K}_+$ can be identified as the point with maximum $\delta\phi_o$ when frequency ω and angle of incidence θ_i are swept in large ranges at a fixed azimuth incidence angle ϕ_i. This phenomenon is a signature of the type-II DPs: as the excited wavevector approaches the DP along the k_x direction, the difference in $v_{g,x}$ for the upper and lower branches changes abruptly. In contrast, away from the DP, such change is gradual. Similar scenario happens when ϕ_i is swept at fixed θ_i and ω, as shown in Fig. 4(d). Therefore, the difference in the azimuth refraction angle $\delta\phi_o$ is a signature of the DPs.

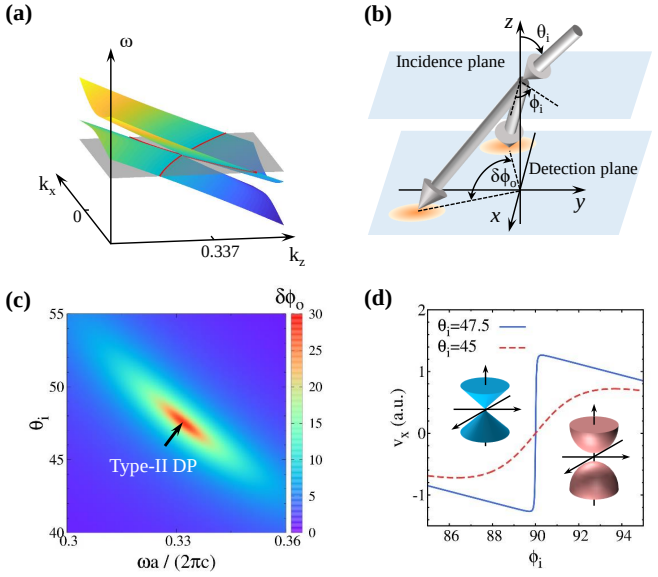

FIG. 4. (Color online) (a) Photonic dispersion near a type-II DP for $l_x = l_y = 0.5$, $w_x = 0.2$, $w_y = 0.3$, $h = 0.25$, and $\varepsilon = 11$. (b) Illustration of the refraction angle measurement. θ_i and ϕ_i are angles of incidence, while $\delta\phi_o$ is the angular difference between the two refraction beams. (c) $\delta\phi_o$ vs. θ_i and ω at $\phi_i = 89.5°$ as a signature of the type-II DP. (d) The group velocity along x direction v_x for the beams correspond to the lower branch as a function of ϕ_i for $\theta_i = 47.5$ (aligned with the DP) and $\theta_i = 45$ (misaligned with the DP).

Conclusion and outlook.— We have shown that the crystalline symmetry of woodpile PCs can enable the emergence of the 3D optical quadratic point and DPs. The DPs exhibit anomalous refraction and birefringence that can enable experimental detection of them. This study offers a guide for the realization of optical Dirac nodal line, FQP and DPs in 3D all-dielectric PCs. It also provides the inspiration and stimulation towards future realization of optical 3D topological insulators in all-dielectric PCs.

Acknowledgments.— HXW and JHJ acknowledge supports from the Jiangsu provincial distinguished professor funding and the National Natural Science Foundation of China (Grant no. 11675116, 11904060, 12074281). JHJ also thanks Zhi Hong Hang, Jie Luo, Zhengyou Liu, and Huanyang Chen for many insightful discussions, as well

as the University of Toronto and the Weizmann Institute of Science for hospitality. YC and HYK are supported by NSERC of Canada Grant No. 06089-2016. HYK acknowledges support from the Canada Research Chairs program.

* gyguo@phys.ntu.edu.tw
† hykee@physics.utoronto.ca
‡ jianhuajiang@suda.edu.cn

[1] G. E. Volovik, *The Universe in a Helium Droplet*, (Oxford: Clarendon Press, 2003).
[2] X. Wan, A. M. Turner, A. Vishwanath, and S. Y. Savrasov, *Topological semimetal and Fermi-arc surface states in the electronic structure of pyrochlore iridates*, Phys. Rev. B **83**, 205101 (2011).
[3] Z. Wang, Y. Sun, X.-Q. Chen, C. Franchini, G. Xu, H. Weng, X. Dai, and Z. Fang, *Dirac semimetal and topological phase transitions in A_3Bi (A = Na, K, Rb)*, Phys. Rev. B **85**, 195320 (2012).
[4] Z. K. Liu, B. Zhou, Y. Zhang, Z. J. Wang, H. M. Weng, D. Prabhakaran, S. K. Mo, Z. X. Shen, Z. Fang, X. Dai, Z. Hussain, and Y. L. Chen, *Discovery of a three dimensional topological Dirac semimetal Na_3Bi*, Science **343**, 864 (2014).
[5] A. A. Soluyanov, D. Gresch, Z. Wang, Q. Wu, M. Troyer, X. Dai, and B. A. Bernevig, *Type-II Weyl semimetals*, Nature (London) **527**, 495 (2015).
[6] B. Bradlyn, J. Cano, Z. Wang, M. G. Vergniory, C. Felser, R. J. Cava, and B. A. Bernevig, *Beyond Dirac and Weyl fermions: unconventional quasiparticles in conventional crystals*, Science **353**, aaf5037 (2016).
[7] N. P. Armitage, E. J. Mele, and Ashvin Vishwanath, *Weyl and Dirac semimetals in three-dimensional solids*, Rev. Mod. Phys. **90**, 015001 (2018).
[8] L. Lu, L. Fu, J. D. Joannopoulos, and M. Soljačić, *Weyl points and line nodes in gyroid photonic crystals*, Nat. Photon. **7**, 294 (2013).
[9] L. Lu, Z. Wang, D. Ye, L. Ran, L. Fu, J. D. Joannopoulos, and M. Soljačić, *Experimental observation of Weyl points*, Science **349**, 622 (2015).
[10] W. Gao, B. Yang, M. Lawrence, F. Fang, B. Béri, and S. Zhang, *Plasmon Weyl degeneracies in magnetized plasma*, Nat. Comm. **7**, 12435 (2016).
[11] D. Wang *et al.*, *Photonic Weyl points due to broken time-reversal symmetry in magnetized semiconductor*, Nat. Phys. **15**, 1150-1155 (2019).
[12] W.-J. Chen, M. Xiao, and C. T. Chan, *Photonic crystals possessing multiple Weyl points and the experimental observation of robust surface states*, Nat. Commun. **7**, 13038 (2016).
[13] H.-X. Wang, L. Xu, H.Y. Chen, and J.-H. Jiang, *Three-dimensional photonic Dirac points stabilized by point group symmetry*, Phys. Rev. B **93**, 235155 (2016).
[14] M. Xiao, Q. Lin, and S. Fan, *Hyperbolic Weyl point in reciprocal chiral metamaterials*, Phys. Rev. Lett. **117**, 057401 (2016).
[15] Q. Lin, M. Xiao, L. Yuan, and S. Fan, *Photonic Weyl point in a two-dimensional resonator lattice with a synthetic frequency dimension*, Nat. Commun. **7**, 13731 (2016).
[16] S. Peng, R. Zhang, V. H. Chen, E. T. Khabiboulline, P. Braun, and H. A. Atwater, *Three-Dimensional Single Gyroid Photonic Crystals with a Mid-Infrared Bandgap*, ACS Photon. **3**, 1131 (2016).
[17] H.-X. Wang, Y. Chen, Z. H. Hang, H.-Y. Kee, and J.-H. Jiang, *Type-II Dirac photons*, npj Quantum Mater. **2**, 54 (2017).
[18] J. Noh, S. Huang, D. Leykam, Y. D. Chong, K. P. Chen, and M. C. Rechtsman, *Experimental observation of optical Weyl points and Fermi arc-like surface states*, Nat. Phys. **13**, 611 (2017).
[19] E. Goi, Z. Yue, B. P. Cumming, and M. Gu, *Observation of type-I Photonic Weyl points in optical frequencies*, Laser & Photon. Rev. **12** 1700271 (2018).
[20] S. Vaidva, J. Noh, A. Cerian, C. Jörg, G. v. Freymann, and M. C. Rechtsman, *Observation of a charge-2 photonic Weyl point in the infrared*, Phys. Rev. Lett. **125**, 253902 (2020).
[21] C. Jörg, S. Vaidva, J. Noh, A. Cerian, S. Augustine, G. v. Freymann, and M. C. Rechtsman, *Observation of the spliting of charge-2 (quadratic) Weyl points in near-infrared photonic crystals*, arXiv: 2106.12119 (2021).
[22] Q. Guo, B. Yang, L. Xia, W. Gao, H. Liu, J. Chen, Y. Xiang, and S. Zhang, *Three dimensional photonic Dirac points in metamaterials*, Phys. Rev. Lett. **119**, 213901 (2017).
[23] M.-L. Chang, M. Xiao, W.-J. Chen, and C. T. Chan, *Multi Weyl points and the sign change of their topological charges in woodpile photonic crystals*, Phys. Rev. B **95**, 125136 (2017).
[24] X. Zhang, *Observing Zitterbewegung for Photons near the Dirac Point of a Two-Dimensional Photonic Crystal*, Phys. Rev. Lett. **100**, 113903 (2008).
[25] R. A. Sepkhanov, Ya. B. Bazaliy, and C. W. J. Beenakker, *Extremal transmission at the Dirac point of a photonic band structure*, Phys. Rev. A **75**, 063813 (2007).
[26] X. Q. Huang, Y. Lai, Z. H. Hang, H. H. Zheng, and C. T. Chan, *Dirac cones induced by accidental degeneracy in photonic crystals and zero-refractive-index materials*, Nat. Mater. **10**, 582 (2011).
[27] M. C. Rechtsman, J. M. Zeuner, A. Tünnermann, S. Nolte, and M. Segev, and A. Szameit, *Strain-induced pseudomagnetic field and photonic Landau levels in dielectric structures*, Nat. Photon. **7**, 153 (2013).
[28] F. D. M. Haldane and S. Raghu, *Possible Realization of Directional Optical Waveguides in Photonic Crystals with Broken Time-Reversal Symmetry*, Phys. Rev. Lett. **100**, 013904 (2008)
[29] Z. Wang, Y. D. Chong, J. D. Joannopoulos, and M. Soljačić, *Reflection-Free One-Way Edge Modes in a Gyromagnetic Photonic Crystal*, Phys. Rev. Lett. **100**, 013905 (2008)
[30] Z. Wang, Y. Chong, J. D. Joannopoulos, and M. Soljačić, *Observation of unidirectional backscattering immune topological electromagnetic states*, Nature **461**, 772-775 (2009).
[31] M. Hafezi, S. Mittal, J. Fan, A. Migdall, and J. M. Taylor, *Imaging topological edge states in silicon photonics*, Nat. Photon. **7**, 1001-1005 (2013).
[32] M. C. Rechtsman *et al.*, *Photonic Floquet topological insulators*, Nature **496**, 196-200 (2013).
[33] A. B. Khanikaev, S. H. Mousavi, W.-K. Tse, M. Kargarian, A. H. MacDonald, and G. Shvets, *Photonic topological insulators*, Nat. Mater. **12**, 233 (2013).

[34] W.-J. Chen, S.-J. Jiang, X.-D. Chen, J.-W. Dong, and C. T. Chan, *Experimental realization of photonic topological insulator in a uniaxial metacrystal waveguide*, Nat. Commun. **5**, 5782 (2014).

[35] T. Ma, A. B. Khanikaev, S. H. Mousavi, and G. Shvets, *Guiding electromagnetic waves around sharp corners: topologically protected photonic transport in metawaveguides*, Phys. Rev. Lett. **114**, 127401 (2015).

[36] L.-H. Wu and X. Hu, *Scheme for Achieving a Topological Photonic Crystal by Using Dielectric Material*, Phys. Rev. Lett. **114**, 223901 (2015).

[37] C. He, X.-C. Sun, X.-P. Liu, M.-H. Lu, Y. Chen, L. Feng, and Y.-F. Chen, *Photonic topological insulator with broken time-reversal symmetry*, Proc. Natl. Acad. Sci. USA **113**, 4924 (2016).

[38] L. Xu, H.-X. Wang, Y.D. Xu, H.Y. Chen, and J.-H. Jiang, *Accidental degeneracy in photonic bands and topological phase transitions in two-dimensional core-shell dielectric photonic crystals*, Opt. Express **24**, 18059 (2016).

[39] L. Lu, C. Fang, L. Fu, S. G. Johnson, J. D. Joannopoulos, and M. Soljačić, *Symmetry-protected topological photonic crystal in three dimensions*, Nat. Phys. **12**, 337 (2016).

[40] A. Slobozhanyuk, S. H. Mousavi, X. Ni, D. Smirnova, Y. S. Kivshar, and A. B. Khanikaev, *Three-dimensional all-dielectric photonic topological insulator*, Nat. Photon. **11**, 130 (2017).

[41] S. Y. Lin, J. G. Fleming, D. L. Hetherington, B. K. Smith, R. Biswas, K. M. Ho, M. M. Sigalas, W. Zubrzycki, S. R. Kurtz, and J. Bur, *A three-dimensional photonic crystal operating at infrared wavelengths*, Nature (London) **394**, 251 (1998).

[42] S. Noda, K. Tomoda, N. Yamamoto, and A. Chutinan, *Full three-dimensional photonic bandgap crystals at near-Infrared wavelengths*, Science **289**, 604 (2000).

[43] M. Deubel, G. von Freymann, M. Wegener, S. Pereira, K. Busch, and C. M. Soukoulis, *Direct laser writing of three-dimensional photonic-crystal templates for telecommunications*, Nat. Mater. **3**, 444 (2004).

[44] S. Noda, M. Fujita, and T. Asano, *Spontaneous-emission control by photonic crystals and nanocavities*, Nat. Photon. **1**, 449-458 (2007).

[45] J. D. Joannopoulos, S. G. Johnson, J. N. Winn, and R. D. Meade, *Photonic crystals: molding the flow of light*, (Princeton university press, 2011).

[46] L. A. Ibbotson, A. Demetriadou, S. Croxall, O. Hess, and J. J. Baumberg, *Optical nano-woodpiles: large-area metallic photonic crystals and metamaterials*, Sci. Rep. **5**, 8313 (2015).

[47] M. I. Shalaev, W. Walasik, A. Tsukernik, Y. Xu, and N. M. Litchinitser, *Robust topologically protected transport in photonic crystals at telecommunication wavelengths*, Nat. Nanotech. **14**, 31 (2019).

[48] P. A. M. Dirac, *The quantum theory of the electron*, Proc. Roy. Soc. A **117**, 610-624 (1928).

[49] See Supplemental Materials.

Supplemental Material for Optical Quadratic and Dirac Points in Woodpile Photonic Crystals

Sec. A Connection between photonic bands in the tetragonal and face-centered cubic Brillouin zones

Here, we illustrate the equivalence of photonic band in the scheme of tetragonal (TET) and face-centered-cubic (FCC) unit-cells under the case with $l_x = l_y = 0.5$. For simplicity, we assume that the all lattice constants along the three directions are 1. As mentioned in the main text, the FCC unit-cell is the primitive unit-cell with only two logs, while the TET unit-cell has four logs. For the TET scheme, the lattice vectors are defined as follows:

$$\vec{b}_1 = (1,\ 0,\ 0), \vec{b}_2 = (0,\ 1,\ 0), \vec{b}_3 = (0,\ 0,\ 1). \tag{10}$$

While for the FCC scheme, we choose the lattice vexctors as follows:

$$\vec{a}_1 = \frac{1}{2}(-\vec{b}_1+\vec{b}_2+\vec{b}_3), \vec{a}_2 = \frac{1}{2}(\vec{b}_1+\vec{b}_2+\vec{b}_3), \vec{a}_3 = \vec{b}_2. \tag{11}$$

Thus $|\vec{a}_1| = |\vec{a}_2| = \frac{\sqrt{3}}{2}$,$|\vec{a}_3| = 1$, and the volume of the FCC unit-cell is $\Omega = |\vec{a}_3 \cdot (\vec{a}_1 \times \vec{a}_2)| = \frac{1}{2}$. It is known to all that the first Brillouin zone reduced by half when the unit-cell is doubled. In order to match the high symmetry points between the TET and FCC Brillouin zone, we need to rotate the unit-cell with 45 degree around $z-axis$, i.e., multiple the lattice vectors with rotation matrix R,

$$\begin{pmatrix} \frac{1}{\sqrt{2}} & \frac{1}{\sqrt{2}} & 0 \\ \frac{1}{\sqrt{2}} & -\frac{1}{\sqrt{2}} & 0 \\ 0 & 0 & 1 \end{pmatrix} \tag{12}$$

Therefore, the new lattice vectors are:

$$\vec{a}_1^{'} = (0,\ -\frac{\sqrt{2}}{2}, \frac{1}{2}), \vec{a}_2^{'} = (\frac{\sqrt{2}}{2},\ 0,\ \frac{1}{2}), \vec{a}_3^{'} = (\frac{\sqrt{2}}{2},\ -\frac{\sqrt{2}}{2},\ 0). \tag{13}$$

Finally, the new reciprocal lattice basis of FCC unit-cell can be derived as:

$$\begin{aligned} \vec{r}_{b1} &= \frac{2\pi}{\Omega}(\vec{a}_2^{'} \times \vec{a}_3^{'}) = 2\pi(\frac{\sqrt{2}}{2}\ \frac{\sqrt{2}}{2}\ -1), \\ \vec{r}_{b2} &= \frac{2\pi}{\Omega}(\vec{a}_3^{'} \times \vec{a}_1^{'}) = 2\pi(-\frac{\sqrt{2}}{2}\ -\frac{\sqrt{2}}{2}\ -1), \\ \vec{r}_{b3} &= \frac{2\pi}{\Omega}(\vec{a}_1^{'} \times \vec{a}_2^{'}) = 2\pi(-\frac{\sqrt{2}}{2}\ \frac{\sqrt{2}}{2}\ 1) \end{aligned} \tag{14}$$

and the correspondence of the high symmetry points between FCC and TET Brillouin zone are list as follows: point Z_0, X_0, W_0 in the Brillouin zone under the FCC scheme refer to the point Γ, M, A in the Brillouin zone under the TET scheme, respectively.

Fig. S1 shows the photonic bands below the fundamental gaps of woodpile in scheme of FCC and TET

unit-cells, respectively. It should be noted there are four bands below the fundamental gap in the TET scheme, while there are only two bands in FCC scheme. In spite of the difference of the amount of the bands in two schemes, we remarked that the equivalence of these two schemes can be verified by band folding analysis. The fourfold degeneracy at the Z point in the scheme of TET unit-cell originates from the band folding.

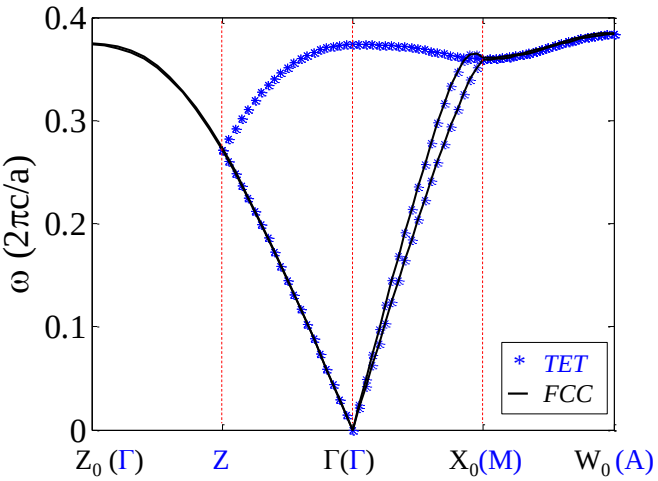

FIG. 5. (Color online) Correspondence of photonic bands of woodpile between two schemes: TET (blue-star) and FCC (black line) unit-cell, respectively. The parameter setting are list as follows: $l_x = l_y = 0.5, w_x = w_y = 0.25, \epsilon = 13$.

Sec. B Symmetries of Woodpile PCs

The other important nonsymmorphic symmetries are the two-fold screw symmetries: $S_x : (x, y, z) \to \left(x + \frac{1}{2}, -y + \frac{1}{2}, -z - \frac{1}{4}\right)$ and $S_y : (x, y, z) \to \left(-x + \frac{1}{2}, y + \frac{1}{2}, -z + \frac{1}{4}\right)$. There are other two glide symmetries: $G_x : (x, y, z) \to (-x, y + \frac{1}{2}, z + \frac{1}{2})$ and $G_y : (x, y, z) \to (x + \frac{1}{2}, -y, z + \frac{1}{2})$.

Sec. C Other Kramers degeneracies

The Kramers degeneracy on the $k_i = \pi (i = x, y)$ plane can be understood via the construction of the anti-unitary operators $\Theta_x \equiv S_x * \mathcal{T} : (x, y, z, t) \to \left(x + \frac{1}{2}, -y + \frac{1}{2}, -z - \frac{1}{4}, -t\right)$ and $\Theta_y \equiv S_y * \mathcal{T} : (x, y, z, t) \to \left(-x + \frac{1}{2}, y + \frac{1}{2}, -z + \frac{1}{4}, -t\right)$, respectively. Let us consider the anti-unitary operator Θ_x as an example. Θ_x transforms $\vec{k}$ to $(-k_x, k_y, k_z)$ is a symmetry operator on the $k_x = \pi$ plane. The square of this operator is $(\Theta_x)^2 : (x, y, z, t) \to (x + 1, y, z, t)$, which yields $(\Theta_x)^2 \Psi_{n,\vec{k}} = e^{ik_x} \Psi_{n,\vec{k}}$ for *all* photonic Bloch states $\Psi_{n,\vec{k}} \equiv (\vec{E}_{n,\vec{k}}, \vec{H}_{n,\vec{k}})^T$ (including both the electric field $\vec{E}$ and the magnetic field $\vec{H}$). Hence for the $k_x = \pi$ plane. Hence, for all Bloch states

$$\Theta_x^2 = e^{ik_x}. \tag{15}$$

Thus on the $k_x = \pi$ plane we have $\Theta_x^2 = -1$ which explains the double degeneracy on the $k_x = \pi$ plane. Specifically, there exist the following commutation relations between anti-unitary operator Θ_x and operator M_x for the $k_x = \pi$ plane,

$$M_x \Theta_x = -\Theta_x M_x. \tag{16}$$

Thus for an eigenstate of M_x with eigenvalue m_x, labeled as $|m_x\rangle$, we have

$$M_x \Theta_x |m_x\rangle = -\Theta_x M_x |m_x\rangle = -m_x \Theta_x |m_x\rangle. \tag{17}$$

Hence $\Theta_x |m_x\rangle$ is also an eigenstate of M_x with opposite eigenvalue. These are the two degenerate Bloch states on the $k_x = \pi$ plane.

In a similar way, the anti-unitary operator Θ_y is a symmetry operator on the $k_y = \pi$ plane. The square of this operator $(\Theta_y)^2 : (x, y, z, t) \to (x, y + 1, z, t)$ yields

$$\Theta_y^2 = e^{ik_y} \tag{18}$$

for all Bloch states. Thus on the $k_y = \pi$ plane we have $\Theta_y^2 = -1$, which yields the Kramers degeneracy.

Moreover, we find that $\Theta_{gx} \equiv G_x * \mathcal{T} : (x, y, z, t) \to (-x, y + \frac{1}{2}, z + \frac{1}{2}, -t)$ and $\Theta_{gy} \equiv G_y * \mathcal{T} : (x, y, z, t) \to (x + \frac{1}{2}, -y, z + \frac{1}{2}, -t)$ can also yield Kramers degeneracy. Since Θ_{gx} transforms $\vec{k}$ into $(k_x, -k_y, -k_z)$, it is a symmetry operator only for the four lines: $k_y, k_z = 0, \pi$. The square of this operator $(\Theta_y)^2 : (x, y, z, t) \to (x, y + 1, z + 1, t)$ yields

$$\Theta_{gx}^2 = e^{i(k_y + k_z)} \tag{19}$$

for all Bloch states. Therefore it leads to double degeneracy for the two lines: $(k_x, 0, \pi)$ and $(k_x, \pi, 0)$. Similarly, Θ_{gy} is a symmetry operator for the four lines: $k_x, k_z = 0, \pi$. The square of this operator $(\Theta_y)^2 : (x, y, z, t) \to (x, y + 1, z + 1, t)$ yields

$$\Theta_{gy}^2 = e^{i(k_x + k_z)} \tag{20}$$

which reuslt in Kramers degeneracy on the two lines: $(0, k_y, \pi)$ and $(\pi, k_y, 0)$. Notice that these lines crossing at the Z point $(0, 0, \pi)$, where both Θ_{gx} and Θ_{gy} are effective.

Sec. D Proof of the fourfold degeneracy on the M-A line

The fourfold degeneracy on the M-A line can be understood as follows: Any Bloch state on this line can be

labeled with the eigenvalues m_x and m_y of the two mirror operators M_x and M_y, respectively. We shall prove that $|m_x, m_y\rangle$, $\Theta_z|m_x, m_y\rangle$ ($\Theta_z \equiv G_z * \mathcal{T}$), $S_\pi|m_x, m_y\rangle$, and $\Theta_z S_\pi|m_x, m_y\rangle$ are distinct from each other. We find that such degeneracy is essentially related to the following commutation relationships on the M-A line,

$$\begin{aligned} &[M_x, \Theta_z]_+ = 0, \quad [M_y, \Theta_z]_- = 0, \\ &[M_x, S_\pi]_+ = 0, \quad [M_y, S_\pi]_+ = 0, \end{aligned} \tag{21}$$

where $[A, B]_\pm = AB \pm BA$. Thus for an eigenstate labeled with m_x and m_y of mirror operator M_x and M_y, we have

$$\begin{aligned} &M_x\Theta_z|m_x, m_y\rangle = -\Theta_z M_x|m_x, m_y\rangle = -m_x\Theta_z|m_x, m_y\rangle, \\ &M_y\Theta_z|m_x, m_y\rangle = \Theta_z M_y|m_x, m_y\rangle = m_y\Theta_z|m_x, m_y\rangle, \\ &M_x S_\pi|m_x, m_y\rangle = -S_\pi M_x|m_x, m_y\rangle = -m_x S_\pi|m_x, m_y\rangle, \\ &M_y S_\pi|m_x, m_y\rangle = -S_\pi M_y|m_x, m_y\rangle = -m_y S_\pi|m_x, m_y\rangle. \end{aligned} \tag{22}$$

From these relations, we find that: (i) $\Theta_z|m_x, m_y\rangle$ is also an eigenstates of M_x with opposite eigenvalue, i.e.,$\Theta_z|m_x, m_y\rangle = |-m_x, m_y\rangle$; (ii) $S_\pi|m_x, m_y\rangle$ is also an eigenstates of $M_x(M_y)$ with opposite eigenvalue, i.e., $S_\pi|m_x, m_y\rangle = |-m_x, -m_y\rangle$. (ii) $\Theta_z S_\pi$ is also an eigenstates of M_y with opposite eigenvalue, i.e., $\Theta_z S_\pi|m_x, m_y\rangle = |m_x, -m_y\rangle$. It is evident that these four states, i.e., $|m_x, m_y\rangle$, $\Theta_z|m_x, m_y\rangle$, $S_\pi|m_x, m_y\rangle$, and $\Theta_z S_\pi|m_x, m_y\rangle$ are distinct from each other and they are related by symmetry operators. Therefore, they are degenerate states.

Sec. E Proof of the fourfold quadratic degeneracy on the Z point

The $S_{\frac{\pi}{2}}$ operator transforms the eigenstate of M_x with the eigenvalue m_x at $\vec{k}$ to a Bloch state at $\vec{k}'$ as the eigenstate of M_y with the same eigenvalue, i.e.,

$$\Theta_{\frac{\pi}{2}} M_x \Theta_{-\frac{\pi}{2}} = M_y. \tag{23}$$

Thus $\Theta_{\frac{\pi}{2}}$ is a symmetry operator only for the Z and A points. Analogous to the Kramers degeneracy, the above yields fourfold degeneracy at the Z point. The four degenerate states are $|\Psi\rangle$, $\Theta_{\frac{\pi}{2}}|\Psi\rangle$, $(\Theta_{\frac{\pi}{2}})^2|\Psi\rangle$, and $(\Theta_{\frac{\pi}{2}})^3|\Psi\rangle$.

The four degenerate states can be labeled by the eigenvalue of M_x, M_y and $\tilde{G}_z = e^{i\frac{\pi}{4}} G_z$. We find that

$$[\Theta_{\frac{\pi}{2}}, \tilde{G}_z]_- = 0, \quad [(\Theta_{\frac{\pi}{2}})^2, \tilde{G}_z]_+ = 0, \tag{24}$$

$$[(\Theta_{\frac{\pi}{2}})^2, M_x]_- = 0, \quad [(\Theta_{\frac{\pi}{2}})^2, M_y]_- = 0. \tag{25}$$

Thus $|\Psi\rangle$ and $\Theta_{\frac{\pi}{2}}|\Psi\rangle$ carry distinct mirror eigenvalues but the same $\tilde{G}_z$ eigenvalue, whereas $|\Psi\rangle$ and $(\Theta_{\frac{\pi}{2}})^2|\Psi\rangle$ carry the same mirror eigenvalues but different $\tilde{G}_z$ eigenvalues. For simplify, we label the Bloch states, which is the eigenstates of M_x, M_y and G_z with eigenvalue m_x, m_y, and g_z, respectively, as $|m_x, m_y, g_z\rangle$. According to the above commute (anticommute) relationships, we find that $\Theta_{\frac{\pi}{2}}|\Psi\rangle = |m_y, m_x, g_z\rangle$, $(\Theta_{\frac{\pi}{2}})^2|\Psi\rangle = |m_x, m_y, -g_z\rangle$, and $(\Theta_{\frac{\pi}{2}})^3|\Psi\rangle = |m_y, m_x, -g_z\rangle$. It is obviously that these four states, i.e., $|m_x, m_y, g_z\rangle$,$|m_y, m_x, g_z\rangle$,$|m_x, m_y, -g_z\rangle$, and $|m_y, m_x, -g_z\rangle$ are distinct from each other and they are related by symmetry operations. Therefore, we prove the fourfold degeneracy at Z point.

Sec. F Varying geometries and materials

Here we show the emergent Dirac physics are robust to the material and geometry of the photonic crystals. We calculate the photonic bands along the high symmetry lines with three different geometric/material parameter settings. The results of the photonic bands are shown in Fig.6, where the Dirac nodal line and the quadratic point holds for all parameters. This is because such double degeneracy are guranteed the lattice symmetry. This also indicates the stableness of the Dirac points and implies that such a symmetry-guided method can also be effective in other classicl/bosonic systems.

Sec. G $\vec{k}\cdot\vec{P}$ Hamiltonian of the Dirac nodal line

The photonic Hamiltonian is obtained by applying the $\vec{k}\cdot\vec{P}$ method to the Maxwell equation,

$$\boldsymbol{\nabla} \times \frac{1}{\varepsilon}\boldsymbol{\nabla} \times \vec{H}_{n',\vec{k}} = \frac{\omega^2_{n',\vec{k}}}{c^2}\vec{H}_{n',\vec{k}}. \tag{26}$$

The photonic Hamiltonian $\hat{\mathcal{H}}_{EM} \equiv c^2\boldsymbol{\nabla}\times\frac{1}{\varepsilon}\boldsymbol{\nabla}\times$ around a high symmetry $\vec{K}$ is obtained as follows. We first expand the Bloch states at a wavevector $\vec{k}$ in the basis formed by the four Bloch states at the high symmetry point, i.e., ($\vec{q} \equiv \vec{k} - \vec{K}$)

$$\vec{H}_{n',\vec{q}} = \sum_n e^{i\vec{q}\cdot\vec{r}} C_n \vec{H}_{n'}, \tag{27}$$

where $\vec{H}_{n'}$ is the magnetic field at the $\vec{q} = 0$ point (i.e., the high symmetry point) and C_n are the coefficients to be solved by diagonalizing the Hamiltonian (and normalized as $\sum_n |C_n|^2 = 1$). The magnetic fields are normalized such that (UC stands for unit-cell)

$$\int_{UC} d\vec{r}\vec{H}^*_n \cdot \vec{H}_{n'} = \delta_{n,n'}. \tag{28}$$

The Hamiltiona is written in the basis of the Bloch states $\vec{H}_{n'}$, and we find that

$$\hat{\mathcal{H}}_{EM} = \omega_0^2\delta_{n,n'} + \sum_\alpha q_\alpha P^\alpha_{n,n'} + \sum_{\alpha,\beta} W_{n\alpha,n'\beta} q_\alpha q_\beta. \tag{29}$$

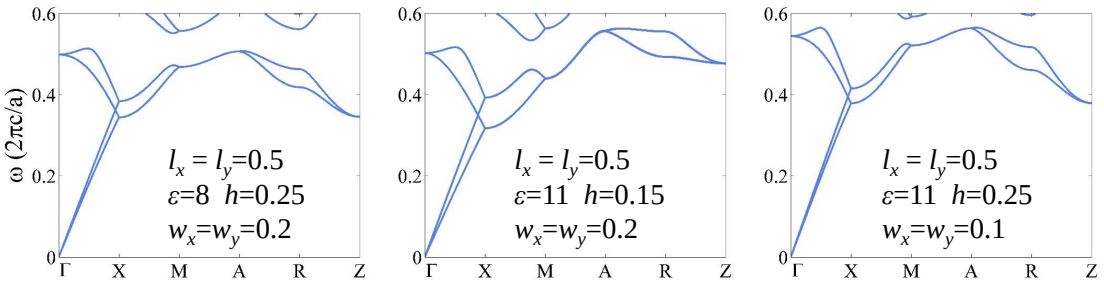

FIG. 6. (Color online) Photonic bands along the high symmetry lines for various geometry/material parameters. (a) $l_x = l_y = 0.5, w_x = w_y = 0.2, h = 0.25, \epsilon = 8$, (b) $l_x = l_y = 0.5, w_x = w_y = 0.2, h = 0.15, \epsilon = 11$, (c) $l_x = l_y = 0.5, w_x = w_y = 0.1, h = 0.25, \epsilon = 11$.

Direct calculation yields,

$$P^{\alpha}_{n,n'} = i\sum_{\nu}\int_{u.c.}\frac{d\vec{r}}{\varepsilon(\vec{r})}[H^*_{n,\nu}\partial_\nu H_{n',\alpha} - H_{n',\nu}\partial_\nu H^*_{n,\alpha} - H^*_{n,\nu}\partial_\alpha H_{n',\nu} + H_{n',\nu}\partial_\alpha H^*_{n,\nu}]. \quad (30)$$

We shall use the Maxwell equation to simplify the above results

$$\partial_\nu H_{n,\alpha} = \sum_{\mu} -i\frac{\omega_n}{c}E_{n,\mu}\epsilon_{\nu\alpha\mu}\varepsilon(\vec{r}), \quad (31)$$

where $\omega_n = \omega_0$ at the degenerate point, $\epsilon_{\nu\alpha\mu}$ is the Levi-Civita tensor, $\vec{E}_n$ is the electric field of the Bloch states at $\vec{q} = 0$ satisfying the normalization condition of

$$\int_{u.c.} d\vec{r}\varepsilon(\vec{r})\vec{E}^*_n \cdot \vec{E}_{n'} = \delta_{n,n'}. \quad (32)$$

Using Eq. (31), we find that

$$P^{\alpha}_{n,n'} = 2\omega_0 c\int_{u.c.} d\vec{r}[\vec{E}_{n'} \times \vec{H}^*_n + \vec{E}^*_n \times \vec{H}_{n'}] \cdot \vec{n}_\alpha \quad (33)$$

where $\alpha = (x, y, z)$ and $\vec{n}_\alpha$ is the unit vector along the α direction. And

$$W_{n\alpha,n'\beta} = c^2\int_{u.c.}\frac{d\vec{r}}{\varepsilon(\vec{r})}[\delta_{\alpha\beta}(\vec{H}^*_n \cdot \vec{H}_{n'}) - H^*_{n\alpha}H_{n'\beta}]. \quad (34)$$

The photonic Hamiltonian $\hat{\mathcal{H}}_{EM}$ is connected with the simulated fermion-like as follows, ($\hbar \equiv 1$)

$$\hat{\mathcal{H}}_{EM} := (\hat{\mathcal{H}}_F)^2. \quad (35)$$

Therefore, near the degenerate point, we have

$$\hat{\mathcal{H}}_F = \omega_0 + \sum_{\alpha}\hat{v}^{\alpha}q_\alpha + \sum_{\alpha,\beta}\hat{w}_{\alpha,\beta}q_\alpha q_\beta + ... \quad (36)$$

where ... represents higher order terms, and

$$\hat{v}^{\alpha} = \frac{1}{2\omega_0}P^{\alpha}_{n,n'},$$
$$\hat{w}_{\alpha,\beta} = \frac{1}{2\omega_0}\hat{W}_{\alpha,\beta}. \quad (37)$$

One can easily verify that $\hat{v}^{\alpha}$ and $\hat{w}_{\alpha,\beta}$ are Hermitian operators.

We now examine the constraints on the matrix element of $\hat{v}$ imposed by the mirror and/or glide symmetry. Explicitly, we have

$$v^{\alpha}_{n,n'} = c\sum_{\mu,\nu}\epsilon_{\alpha\mu\nu}\int_{u.c.} d\vec{r}[E_{n',\mu}H^*_{n,\nu} + E^*_{n,\mu}H_{n',\nu}]. \quad (38)$$

If, say, there is a mirror or glide symmetry, labeled as $\hat{F}_x$, the mirror operation acts on the electric and magnetic fields as follows:

$$\begin{aligned}
\hat{F}_x H_x(\vec{r}) &= H_x(\hat{F}_x\vec{r}),\\
\hat{F}_x H_y(\vec{r}) &= -H_y(\hat{F}_x\vec{r}),\\
\hat{F}_x H_z(\vec{r}) &= -H_z(\hat{F}_x\vec{r}),\\
\hat{F}_x E_x(\vec{r}) &= -E_x(\hat{F}_x\vec{r}),\\
\hat{F}_x E_y(\vec{r}) &= E_y(\hat{F}_x\vec{r}),\\
\hat{F}_x E_z(\vec{r}) &= E_z(\hat{F}_x\vec{r}).
\end{aligned} \quad (39)$$

Thus, the velocity matrix element $v^{\alpha}_{n,n'}$ is nonzero only when the n and n' states carry opposite mirror eigenvalue m_α (or glide eigenvalue g_α).

The invariance of the Hamiltonian under a symmetry operation $\mathcal{S}$ implies that

$$\mathcal{S}\mathcal{H}(\vec{k})\mathcal{S}^{-1} = \mathcal{H}(\mathcal{S}\vec{k}). \quad (40)$$

For example, the time-reversal symmetry symmetry $\mathcal{T} = -\mathcal{K}$ yields that the $\vec{k}\cdot\vec{P}$ around a time-reversal invariant momentum has

$$(v^{\alpha}_{n,n'})^* = -v^{\alpha}_{n,n'} \quad (41)$$

Hence the matrix element of the q linear terms are purely imaginary. One can prove that the q quadratic terms are purely real.

We now derive the $\vec{k}\cdot\vec{P}$ Hamiltonian for the Dirac nodal line. Around a point on the M-A line, the four degenerate states are chosen as the $|m_x, m_y\rangle$ for $m_x, m_y = \pm 1$.

In the basis of $(|1,1\rangle, |-1,-1\rangle, |-1,1\rangle, |1,-1\rangle)^T$ the q linear Hamiltonian is written as

$$\hat{\mathcal{H}}_F^{DL} = \omega_0 + \begin{pmatrix} 0 & 0 & a_1 q_x & a_2 q_y \\ 0 & 0 & b_1 q_y & b_2 q_x \\ a_1^* q_x & b_1^* q_y & 0 & 0 \\ a_2^* q_y & b_2^* q_x & 0 & 0 \end{pmatrix}, \tag{42}$$

where a_i and b_i are the $\vec{k}\cdot\vec{P}$ coefficients which can be calculated from the photonic Bloch functions $\vec{H}_n$ at the degeneracy point (π, π, k_z) (hence these coefficients are k_z dependent). Those coefficients are restricted by the symmetry via Eq. (40). Two symmetry operations are relevant: Θ_z and S_π. In the chosen basis, these operations are manifested as the following matrices:

$$\Theta_z = \tau_y \mathcal{K}, \quad S_\pi = \sigma_y e^{ik_z z/2}. \tag{43}$$

Their effects on the wavevectors are

$$\Theta_z \vec{k} = (-k_x, -k_y, k_z), \quad S_\pi \vec{k} = (-k_x, -k_y, k_z). \tag{44}$$

We thus obtain from Eq. (40) that

$$b_1 = a_2, \quad b_2 = -a_1. \tag{45}$$

It is convenient to define $v = \sqrt{|b_1|^2 + |b_2|^2} = \sqrt{|a_1|^2 + |a_2|^2}$, $\gamma_x = a_1/v$, and $\gamma_y = a_2/v$. In the new basis of $(|\uparrow, p\rangle, |\downarrow, p\rangle, |\uparrow, a\rangle, |\downarrow, a\rangle)^T$, the $\vec{k}\cdot\vec{P}$ Hamiltonian can be further simplified as

$$\hat{\mathcal{H}}_F^{DL} = \omega_0 + v \begin{pmatrix} 0 & \hat{\mathcal{A}} \\ \hat{\mathcal{A}}^\dagger & 0 \end{pmatrix} + \mathcal{O}(q^2),$$
$$\hat{\mathcal{A}} \equiv \gamma_x q_x \sigma_x + \gamma_y q_y \sigma_y. \tag{46}$$

The above Hamiltonian applies for the whole M-A line, where the coefficients ω_0, v, γ_x and γ_y are k_z-dependent. At the M or A point, the S_4 symmetry also holds, thus there will be additional constraints on the coefficients. Let's consider such constraints in the original basis for the Hamiltonian Eq. (42). S_4 is manifested as $-\sigma_0$ in the even-parity doublet, whereas $S_4 = -i\sigma_y$ in the odd-parity doublet. Imposing (40) we find that for the M and A points, $\gamma_x = \gamma_y$. In addition, for these points, the time-reversal symmetry dictates that $\gamma_x = \gamma_y$ are purely imaginary coefficients. Therefore, at these points the Dirac point is doubly degenerate in the k_x-k_y plane, while away from these points the dispersion in the k_x-k_y plane is generally non-degenerate. The double degeneracy for generic points on the MA line (except the M and A points) are restored only for $q_x = 0$ or $q_y = 0$ (i.e., at the $k_x = \pi$ or $k_y = \pi$ plane), where the nonsymmorphic screw symmetry ensures double degeneracy.

For the quadratic degeneracy at the Z point, the eigenstates can be labeled as $|m_x, m_y, g_z\rangle$ for $m_x = -m_y = \pm 1, g_z = \pm 1$. Using the basis of $(|-1,1,1\rangle, |1,-1,1\rangle, |-1,1,-1\rangle, |1,-1,-1\rangle)^T$, the q linear term comes simply as $v_z q_z \tau_y$, because it is finite only between states with opposite g_z. Considering the $S_{\frac{\pi}{2}}$ symmetry, the higher order terms are

$$f_0 f_2 q_\parallel^2 + f_0 \begin{pmatrix} q_x^2 - q_y^2 & 2f_1 q_x q_y & 0 & 0 \\ 2f_1 q_x q_y & q_y^2 - q_x^2 & 0 & 0 \\ 0 & 0 & q_x^2 - q_y^2 & 2f_1 q_x q_y \\ 0 & 0 & 2f_1 q_x q_y & q_y^2 - q_x^2 \end{pmatrix}. \tag{47}$$

The above Hamiltonian recovers Eq. (8) in the main text when written in the basis of spin states that carrying angular momentum. When the $S_{\frac{\pi}{2}}$ symmetry is broken the degeneracy between states with different m_x at $q_z = 0$ is split by a constant term $\Delta_z f_0 \sigma_z$ with Δ_z characterizing the strength of the perturbation.

Sec. H Optical properties of type-II Dirac points

The type-II DPs offer special band structures that may enable in the manipulation of light in ways that cannot be achieved in uniform dielectric materials. The refraction properties can be determined by matching the frequency and the wavevector parallel to the interface. Here, we consider refraction on the (001) surface where light is injected from air (above the PC). The wavevector in the air is determined by the frequency and angle of incidence (θ_i and ϕ_i) via

$$k_x = \frac{\omega}{c}\sin\theta_i \cos\phi_i, \quad k_y = \frac{\omega}{c}\sin\theta_i \sin\phi_i,$$
$$k_z = \frac{\omega}{c}\cos\theta_i. \tag{48}$$

The wavevector k_x and k_y remains the same in the PC, the quantity to be found is the wavevector along z direction in the PC. We shall denote the wavevector in the PC as $\vec{q}$. So far we have

$$q_x = k_x, \quad q_y = k_y. \tag{49}$$

For the Dirac points, q_z is obtained by solving the equation,

$$\delta\omega = v_z q_z \tau_z + f_0 \left[\beta q_\parallel^2 \pm \sqrt{(\Delta_z + q_x^2 - q_y^2)^2 + 4 q_x^2 q_y^2} \right],$$

for the $\pm$ branches with $\tau_z = -1$ as required by that the group velocity along the z direction should be negative. The above equation can be solved straightforwardly.

The group velocity along the x and y directions are then,

$$\begin{aligned} v_{g,x} &= \frac{\partial \omega}{\partial q_x} = f_0 \left(2\beta q_x \pm \frac{2(\Delta_z + q_x^2 - q_y^2) q_x + 4 q_y^2 q_x}{\sqrt{(\Delta_z + q_x^2 - q_y^2)^2 + 4 q_x^2 q_y^2}} \right), \\ v_{g,y} &= \frac{\partial \omega}{\partial q_y} = f_0 \left(2\beta q_y \pm \frac{-2(\Delta_z + q_x^2 - q_y^2) q_y + 4 q_x^2 q_y}{\sqrt{(\Delta_z + q_x^2 - q_y^2)^2 + 4 q_x^2 q_y^2}} \right). \end{aligned} \tag{50}$$

The refraction angle ϕ_o is then determined as

$$\phi_o = \mathrm{Arg}[v_{g,x} + i v_{g,y}] \tag{51}$$

for the $\pm$ branches. The crucial physics is that around the type-II Dirac point the $v_{g,x}$ becomes significant for the two branches and they are of opposite sign, while the $v_{g,y}$ do not change significantly. This yields a large variation of the refraction angle across the Dirac point, such variation goes to opposite direction for the two branches.